Algebraic dynamic multilevel (ADM) method for CO$_2$ storage in heterogeneous saline aquifers

Zhao, Mengjie; Gerritsma, Marc; Al Kobaisi, Mohammed; Hajibeygi, Hadi

Important note
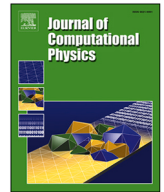To cite this publication, please use the final published version (if applicable).
Please check the document version above.

Algebraic dynamic multilevel (ADM) method for CO_2 storage in heterogeneous saline aquifers

Mengjie Zhao [ID] [a,*], Marc Gerritsma [a], Mohammed Al Kobaisi [b], Hadi Hajibeygi [c]

[a] *Faculty of Aerospace Engineering, Department of Flow Physics and Technology, Delft University of Technology, Kluyverweg 2, 2629 HS, Delft, The Netherlands*
[b] *Faculty of Electrical Engineering, Mathematics, and Computer Science, Department of Applied Mathematics, Delft University of Technology, Mekelweg 4, 2628 CD, Delft, The Netherlands*
[c] *Faculty of Civil Engineering and Geosciences, Department of Geoscience and Engineering, Delft University of Technology, Stevinweg 1, 2628 CV, Delft, The Netherlands*

ARTICLE INFO

ABSTRACT

This work introduces a novel application of the Algebraic Dynamic Multilevel (ADM) method for simulating CO_2 storage in deep saline aquifers. By integrating a fully implicit coupling strategy, fully compositional thermodynamics, and adaptive mesh refinement, the ADM framework effectively models phenomena such as buoyancy-driven migration, convective dissolution, and phase partitioning under various subsurface conditions. The method starts with the construction of a hierarchy of multilevel grids and the generation of localized multiscale basis functions, which account for heterogeneities at each coarse level. During the simulation, the ADM method dynamically refines areas with significant overall CO_2 mass fraction gradients while coarsening smooth regions, thus optimizing computational resources without compromising the accuracy required to capture essential flow and transport characteristics. This dynamic grid adjustment is facilitated by algebraic prolongation and restriction operators, which map the fine-scale system onto a coarser grid suited to the evolving distribution of the CO_2 plume. This feature allows the ADM to navigate various coarsening thresholds efficiently, striking a trade-off between computational economy and detailed simulation accuracy. Even at relatively higher thresholds, key trapping mechanisms are captured with sufficient detail for quantification. These capabilities make the ADM framework well suited for long-term CO_2 sequestration in highly heterogeneous reservoirs, where large-scale models may otherwise become impractically expensive, offering a practical balance between the need for detailed simulations and manageable computational requirements. Overall, the ADM framework proves to be a robust tool for designing, monitoring, and analyzing large-scale CO_2 storage operations, supporting reliable and cost-effective solutions in carbon management.

1. Introduction

Carbon capture and storage (CCS) is a promising technology for mitigating greenhouse gas emissions by sequestering CO_2 from fossil fuel sources [1,2]. In a typical CCS operation, the compressed supercritical CO_2 is injected into suitable geological formations, such as depleted hydrocarbon reservoirs and deep saline aquifers [3,4]. Saline aquifers are particularly attractive for large-scale

CO_2 storage because of their extensive pore space and broad geographic distribution, providing a reliable and secure long-term CO_2 sequestration option [5–7]. Once injected, supercritical CO_2 is immiscible with the resident brine. As CO_2 dissolves in the brine, it increases the density of brine, thus reducing the risk of CO_2 migration upwards [8].

Accurately simulating the behavior of CO_2 under various forces in different subsurface structures is important for effective CCS strategy optimization [9] and risk assessment [10]. However, the interplay between strongly heterogeneous properties of rock (e.g. permeability) and the complex and coupled multiphase, multicomponent dynamics of CO_2 and brine complicate the prediction of the CO_2 plume migration [11–13]. Currently, numerical simulation is the primary tool for modeling the CO_2 migration by solving the high-fidelity discretizations of mass and energy conservation equations governing the dynamics of multiphase, multicomponent flows [14,15]. Such simulations typically account for buoyancy-driven flow, dissolution, diffusion, and capillary effects to provide insights into the key trapping mechanisms that influence CO_2 distribution in the formation.

Several classical numerical methods have been employed for these tasks, including the finite volume method (FVM), the finite element method (FEM), and the lattice Boltzmann Method (LBM). FVM is widely adopted for flow and transport problems [16], FEM is commonly used for structural analyses [17], and LBM is particularly effective for microscale fluid dynamics [18]. In the context of CO_2 storage, FVM is frequently employed due to its efficiency and ability to handle conservation laws in large-scale reservoir models [19,20]. Additional developments include parameterization of reactive-compositional flows [21], fully implicit methods for two-phase reactive flows [22], and advanced thermodynamic models that account for temperature and capillary transition effects [23]. High-resolution simulations also enable the monitoring of CO_2 migration after injection [24].

Despite these advances, the high-resolution grids required to accurately capture flow physics and geological heterogeneity often exceed the capabilities of classical numerical approaches [25]. Grids at the Darcy scale (on the order of centimeters) can generate extremely large linear systems, leading to the conventional methods becoming impractical for field-scale applications. Consequently, there is a demand for advanced numerical techniques that can preserve fine-scale details while ensuring computational efficiency.

One class of solutions involves multiscale methods, such as the multiscale finite element (MsFE) [26,27] and multiscale finite volume (MsFV) approaches [28,29]. These methods construct coarse-scale pressure systems while preserve critical fine-scale information through locally computed basis functions. Algebraic restriction and prolongation operators then map the coarse-scale solution back to the original high-resolution grid, allowing an approximate solution that captures essential flow details without globally refining the entire domain [11]. The MsFV method has been particularly effective for sequential simulations of flow and transport, where the coarse-scale pressure solution is used to reconstruct fine-scale conservative velocities, followed by transport calculations [30,31]. For fully implicit (FIM) formulations, where flow and transport equations are solved simultaneously, such reconstruction introduces additional complexity. Building on these concepts, the Algebraic Dynamic Multilevel (ADM) method was introduced to handle FIM systems on dynamically updated multilevel grids [32,33]. ADM addresses the multiscale multilevel coexistence of pressure (elliptic or parabolic) and transport (hyperbolic) unknowns by adaptively refining or coarsening the mesh at each time step based on a front-tracking criterion, thus focusing fine-scale resolution only where significant gradients and physical interactions occur. It benefits from the consistent basis function structure of MsFE and MsFV while avoiding the reconstruction of conservative fields, as the transport equations are solved on the adaptive grid. Mass conservation is enforced at every level by carefully designed finite-volume restriction operators, while pressure and transport variables are interpolated using multiscale and constant basis functions, respectively. This strategy reduces computational costs significantly, and maintains a high level of accuracy even in highly heterogeneous media. In previous work, ADM was developed for two-phase immiscible displacement and black-oil models in heterogeneous reservoirs [34,35].

In the context of CCS, ADM offers potential for modeling CO_2 storage because its dynamic refining strategy effectively addresses localized heterogeneities that can strongly influence plume migration and trapping mechanisms. Recognizing these advantages, we extend ADM in this work to capture the complexities of multiphase, multicomponent flow by incorporating gravitational and capillary forces, as well as phase partitioning. We employ an overall-composition formulation in which primary unknowns are mapped from the fine-scale grid to a dynamically refined grid. The grid resolution is determined by the differences in component mass fractions between neighboring cells, ensuring that regions with large gradients receive finer discretization. This dynamic and scalable framework is particularly suitable for long-term CO_2 storage, where flow dynamics evolve over time. In this paper, we apply ADM to simulate CO_2 storage in deep saline aquifers, and demonstrate improved simulation performance relative to fully refined grids, including for challenging scenarios such as the SPE11 benchmark [36].

The remaining sections of the paper are organized as follows. The fine-scale formulations and solution strategy for CO_2 storage in saline aquifers are described in Section 2. The ADM method as a simulation strategy for CO_2 storage is described in Section 3. Numerical results for the test case and benchmark studies are presented in Section 4. Section 5 concludes with the observations as well as the outlook for future studies.

2. Fine-scale model and solution strategy

2.1. Governing equations

In the context of CO_2 sequestration in saline aquifers, the mass conservation equation governing the n_{ph} phases and n_c components is formulated as [37]:

$$\frac{\partial}{\partial t}\left(\phi \sum_{\alpha=1}^{n_{ph}} x_{c,\alpha} \rho_\alpha S_\alpha\right) + \nabla \cdot \sum_{\alpha=1}^{n_{ph}} \left(x_{c,\alpha} \rho_\alpha \mathbf{u}_\alpha + S_\alpha \rho_\alpha \mathbf{J}_{c,\alpha}\right) - \sum_{\alpha=1}^{n_{ph}} x_{c,\alpha} q_\alpha = 0, \tag{1}$$

where t is the time variable, and ϕ is the porosity of the medium. The subscript $\alpha \in \{w, n\}$ denotes the wetting (brine-rich) and non-wetting (CO_2-rich) phases. The index c represents the components (CO_2 and H_2O). The parameters ρ_α, S_α, and q_α denote the density, saturation, and source or sink terms of phase α, respectively. $x_{c,\alpha}$ is the mass fraction of component c in phase α. The phase velocity $\mathbf{u}_\alpha$ follows Darcy's law:

$$\mathbf{u}_\alpha = -\frac{\mathbf{k} k_{r,\alpha}}{\mu_\alpha}(\nabla P_\alpha + \rho_\alpha \mathbf{g}), \tag{2}$$

where $\mathbf{k}$ is the rock permeability. $k_{r,\alpha} = k_{r,\alpha}(S_\alpha)$ and μ_α are the phase relative permeability and viscosity, respectively. $\mathbf{g}$ is the gravitational acceleration vector. Additionally, the diffusion flux $\mathbf{J}_{c,\alpha}$ is described by Fick's law, accounting for molecular diffusion driven by gradients of the component mass fraction:

$$\mathbf{J}_{c,\alpha} = -\phi D_{c,\alpha} \nabla x_{c,\alpha}, \tag{3}$$

where $D_{c,\alpha}$ is the mutual diffusion coefficient of component c in phase α. Moreover, the phase pressures P_α are related to the capillary pressure P_c which depends on the saturation:

$$P_n - P_w = P_c(S_w), \tag{4}$$

In addition, the model assumes that the pore space is fully occupied by the phases, with CO_2 and H_2O accounting for all component distributions. This is mathematically enforced by the conditions that the sum of phase saturations and component mass fractions in each phase equal one:

$$\sum_{\alpha=w,n} S_\alpha = 1, \text{ and } \sum_{c=CO_2,H_2O} x_{c,\alpha} = 1. \tag{5}$$

2.2. Fully compositional thermodynamics

In deep saline aquifers, injected CO_2 interacts with resident brine, forming a multiphase system typically comprising an aqueous phase and a supercritical or gaseous CO_2-rich phase. Accurate modeling of this system requires a thermodynamic description of phase equilibrium that accounts for pressure, temperature, and salinity. Thermodynamic equilibrium governs the partitioning of chemical species across coexisting phases and provides the foundation for compositional simulation and solubility modeling. For a binary CO_2-H_2O system, thermodynamic equilibrium is achieved when the fugacity of each component is equal in both phases:

$$f_{c,\alpha}(p, x_{c,\alpha}) - f_{c,\beta}(p, x_{c,\beta}) = 0, \quad \forall \alpha \neq \beta \in \{1, \ldots, n_{ph}\}, \; c \in \{CO_2, H_2O\}, \tag{6}$$

where $f_{c,\alpha}$ is the fugacity of component c in phase α. This condition is often reformulated in terms of equilibrium ratios, or K-values:

$$K_c = \frac{x_{c,n}}{x_{c,w}}, \tag{7}$$

where $x_{c,n}$ and $x_{c,w}$ are the mass fractions of component c in the vapor and aqueous phases, respectively. These K-values are functions of pressure, temperature, and salinity, and provide the basis for equilibrium-based compositional modeling. Once K-values are evaluated, phase partitioning is determined by solving the Rachford-Rice equation for vapor fraction V [38]:

$$\sum_{c=1}^{n_c} \frac{z_c(K_c - 1)}{1 + V(K_c - 1)} = 0, \tag{8}$$

where z_c is the overall mass fraction of component c, i.e.

$$z_c = \frac{\displaystyle\sum_{\alpha=1}^{n_{ph}} x_{c,\alpha} \rho_\alpha S_\alpha}{\displaystyle\sum_{\alpha=1}^{n_{ph}} \rho_\alpha S_\alpha}, \tag{9}$$

To illustrate typical H_2O-CO_2 phase partitioning, Fig. 1 shows how their mutual solubility changes with pressure and temperature, based on model from [39]. At high pressures, where CO_2 exists in a dense phase, its solubility exhibits minimal variation with changes in pressure. In contrast, at low pressures, CO_2 tends to stay primarily in a vapor phase, which correlates with a higher mass fraction of H_2O in the CO_2-rich phase. Increasing pressure within this lower range induces a transition of CO_2 from vapor to a denser phase, leading to a pronounced reduction in H_2O solubility. Additionally, rising temperatures increase the solubility of H_2O in the CO_2-rich phase due to increased water volatility, while simultaneously decreasing CO_2 solubility in H_2O-rich phases.

Furthermore, the impact of mutual solubility on the density of brine is evaluated using:

$$\frac{1}{\rho_w(p_w, T, x_{CO_2,w})} = \frac{1 - x_{CO_2,w}}{\rho_w(p_w, T)} + \frac{x_{CO_2,w}}{\rho_{n,\phi}(T)}, \tag{10}$$

where T is the temperature in Celsius, and M_{CO_2} is the molar weight of CO_2. $\rho_{n,\phi}$ refers to the apparent density of CO_2 dissolved in water [40]. The densities of the CO_2-rich phase and the H_2O-rich phase, spanning conditions from the surface to the reservoir, are illustrated in Fig. 2. The density of the gas phase is unaffected by changes in composition. However, changes in phase composition
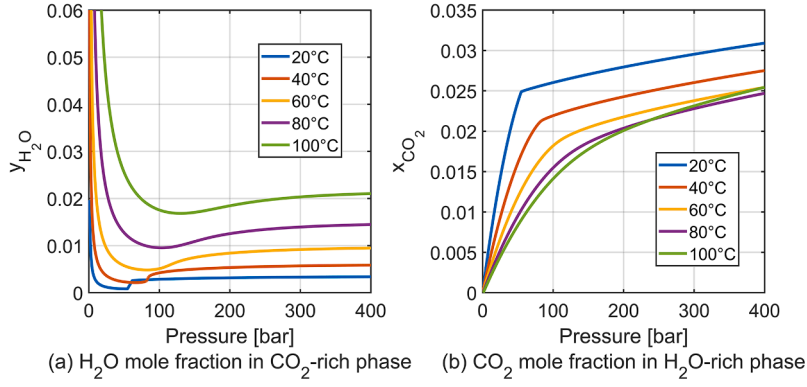
Fig. 1. Mutual solubilities of H_2O and CO_2 from 20 to 100 °C and up to a pressure of 400bar, based on data from [39].
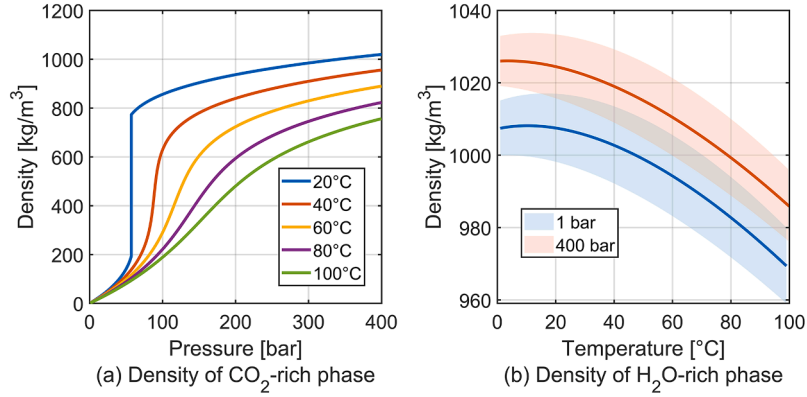

Fig. 2. Density variations in CO_2-rich and H_2O-rich phases under different conditions.

significantly impact the density of H_2O, which in turn influences the migration path of the CO_2 plume. As depicted in Fig. 2(b), the solid line represents the density curve at a CO_2 mass fraction of 0.05 under corresponding pressures, with the shaded background indicating density variations from a CO_2 mass fraction of 0 to 0.1. This variation in density due to CO_2 solubility in water is a critical factor driving gravity-induced currents, leading to the formation of fingering patterns that significantly contribute to CO_2 trapping through dissolution.

2.3. Fine-scale overall-composition formulation

The nonlinear coupled system of equations introduced in the previous section is discretized spatially using a FVM and temporally with a fully implicit scheme. We employ an overall-composition approach in which the wetting-phase pressure (p_w) and the overall mass fraction of CO_2 (z_{CO_2}) serve as the primary variables. In this framework, each grid cell stores these variables and updates them at each time step, ensuring that both pressure and component distributions are captured consistently at the fine scale.

To implement the fully implicit scheme, all terms dependent on p_w and z_{CO_2} are evaluated at the new time step $t + 1$. Consequently, the residual r_c^{t+1} for each component c in cell $\langle i \rangle$ at each time-step must be zero:

$$
\begin{aligned}
r_{c,\langle i \rangle}^{t+1} = & \frac{V_{\langle i \rangle} \phi_{\langle i \rangle}}{\Delta t} \sum_{\alpha=1}^{n_{\text{ph}}} \left(x_{c,\alpha,\langle i \rangle}^{t+1} \rho_{\alpha,\langle i \rangle}^{t+1} S_{\alpha,\langle i \rangle}^{t+1} - x_{c,\alpha,\langle i \rangle}^{t} \rho_{\alpha,\langle i \rangle}^{t} S_{\alpha,\langle i \rangle}^{t} \right) \\
& + \sum_{j=1}^{N_n} \sum_{\alpha=1}^{n_{\text{ph}}} \left(x_{c,\alpha} \rho_\alpha \mathbf{u}_\alpha + S_\alpha \rho_\alpha \mathbf{j}_{c,\alpha} \right) \Big|_{\langle ij \rangle}^{t+1} \cdot \vec{\mathbf{n}} \\
& - \sum_{\alpha=1}^{n_{\text{ph}}} x_{c,\alpha,\langle i \rangle}^{t+1} q_{\alpha,\langle i \rangle}^{t+1} = 0,
\end{aligned}
\tag{11}
$$

where t and $t + 1$ denote the previous and current time steps, respectively. N_n is the number of neighboring cells of cell i and $\vec{\mathbf{n}}$ is the unit normal vector to its boundary. To solve these equations, the Newton-Raphson method is employed to linearize the system

iteratively, i.e.

$$r_c^{v+1} \approx r_c^v + \left.\frac{\partial r_c}{\partial p_w}\right|_v \delta p_w^{v+1} + \left.\frac{\partial r_c}{\partial z_{CO_2}}\right|_v \delta z_{CO_2}^{v+1}, \tag{12}$$

where v and $v+1$ indicate the iteration steps. δp_w^{v+1} and $\delta z_{CO_2}^{v+1}$ are the updates of the unknowns at iteration $v+1$. This leads to a system of linearized equations that can be expressed in a matrix form:

$$\underbrace{\begin{bmatrix} J_{CO_2,p_w}^v & J_{CO_2,z_{CO_2}}^v \\ J_{H_2O,p_w}^v & J_{H_2O,z_{CO_2}}^v \end{bmatrix}}_{\mathbf{J}^v} \underbrace{\begin{bmatrix} \delta p_w^{v+1} \\ \delta z_{CO_2}^{v+1} \end{bmatrix}}_{\delta\xi^{v+1}} = -\underbrace{\begin{bmatrix} r_{CO_2}^v \\ r_{H_2O}^v \end{bmatrix}}_{r^v}. \tag{13}$$

Here, $\mathbf{J}^v$ is the Jacobian (derivatives) matrix, $\delta\xi^{v+1}$ is the vector of unknown increments, and r^v is the residual vector. Because the overall-composition approach tracks the overall mass fraction of CO_2, phase partitioning is determined by thermodynamic equilibrium constraints. If a cell is predicted to be single-phase, certain elements in the Jacobian vanish, simplifying the local flow equations. Conversely, if two phases coexist, the negative flash calculation accurately allocates the CO_2 between the wetting and non-wetting phases. In this way, the Jacobian automatically accommodates changes in phase presence. Then, the linear system is solved iteratively until the convergence criteria (small changes in pressure and overall mass fraction, or sufficiently low residual norms) are met. In this work, a residual tolerance of 10^{-5} and a solution update tolerance of 10^{-4} are used. Furthermore, the initial and maximum time-step sizes are specified by the user. During the FIM simulation, if the number of Newton iterations exceeds It_{max}, the time-step size is halved and the system solved again. A maximum of 10 time-step chops is allowed.

3. ADM method for CO_2 storage

The ADM enhances computational efficiency in CO_2 storage simulations by dynamically adjusting grid resolutions in response to evolving flow characteristics, such as the sharp CO_2 fronts and well boundaries. This strategy allows for manageable simulations while preserving the fine-scale details accurately.

3.1. Adaptive selection of multilevel grids

A key feature of ADM is its ability to refine or coarsen the grid at each time step according to a predefined front-tracking criterion. Rather than starting with a single static mesh, ADM focuses computational resources on cells that exhibit steep gradients in the primary unknown z_{CO_2}. Specifically, at each time step t, the grid for the next time step $t+1$ is selected based on the solution at time step t. The strategy compares the maximum difference in z_{CO_2} between two neighboring coarse blocks Ω_l^I and Ω_l^J at coarse level l. Let i and j index the fine-scale cells belonging to the coarse blocks Ω_l^I and Ω_l^J, respectively. The maximum difference is calculated as:

$$\Delta z_{I,J} = \max_{i\in\Omega_l^I, \, j\in\Omega_l^J} \left| z_i - z_j \right|, \tag{14}$$

If $\Delta z_{I,J}$ for any neighboring coarse blocks exceeds a specified tolerance, the block I is refined from coarse level l to $(l-1)$. Cells surrounding injection wells also remain at the finest resolution to ensure accurate calculations where fluxes are greatest.

For a three-dimensional aquifer, the initial physical domain is often discretized into $N_f = N_{fx} \times N_{fy} \times N_{fz}$ cells, sufficiently refined to capture key CO_2-brine interactions. Although this fully resolved grid can represent the dynamics in detail, running a fully implicit solver across all cells would be impractical for large-scale reservoirs. To address this, ADM constructs a hierarchical series of up to n_l coarser grids, with $l=0$ denoting the finest mesh and higher l corresponding to progressively coarser resolutions. At grid level l, there are $N_l = N_{lx} \times N_{ly} \times N_{lz}$ control volumes, and the coarsening ratio γ^l is defined as:

$$\gamma^l = (\gamma_x^l, \gamma_y^l, \gamma_z^l) = \left(\frac{N_x^{l-1}}{N_x^l}, \frac{N_y^{l-1}}{N_y^l}, \frac{N_z^{l-1}}{N_z^l} \right), \tag{15}$$

Intermediate levels can also be generated to form a nested hierarchy from the finest to the coarsest grids. To maintain smooth transitions, the level difference between neighboring cells is limited to one, preventing sudden changes in resolution that might degrade solution quality.

3.2. Solution strategy

In ADM, the fully-implicit system on the fine grid is transformed to a selected coarser level l by restriction and prolongation operators:

$$\underbrace{\hat{\mathbf{R}}_l^{l-1} \cdots \hat{\mathbf{R}}_1^0 \mathbf{J} \hat{\mathbf{P}}_0^1 \cdots \hat{\mathbf{P}}_{l-1}^l}_{\mathbf{J}_{ADM}} \delta\xi_l^{ADM} = -\underbrace{\hat{\mathbf{R}}_l^{l-1} \cdots \hat{\mathbf{R}}_1^0 r_f}_{r_{ADM}}, \tag{16}$$

where $\mathbf{J}$ and r_f are the Jacobian matrix and residual vector at the fine scale, respectively, and $\delta\xi_l^{\text{ADM}}$ is the solution at grid level l. Restriction operators $\hat{\mathbf{R}}_l^{l-1}$ map residuals of governing equations from level $l-1$ to level l, while the prolongation operators $\hat{\mathbf{P}}_{l-1}^l$ interpolate the solution in the reverse direction. Both $\mathbf{R}$ and $\mathbf{P}$ are block-diagonal matrices:

$$\mathbf{R}_l^{l-1} = \begin{pmatrix} (R_p)_l^{l-1} & \mathbf{0} \\ \mathbf{0} & (R_z)_l^{l-1} \end{pmatrix}_{N_l \times N_{l-1}}, \tag{17}$$

and

$$\mathbf{P}_{l-1}^l = \begin{pmatrix} (P_p)_{l-1}^l & \mathbf{0} \\ \mathbf{0} & (P_z)_{l-1}^l \end{pmatrix}_{N_{l-1} \times N_l}, \tag{18}$$

Here, the subscript p and z denote the pressure and overall mass fraction sub-blocks, respectively. The same finite-volume restriction operator is typically applied to both variables to ensure the local mass balance, meaning $(R_p)_l^{l-1} = (R_z)_l^{l-1}$. Specifically, each entry of the restriction operator $(R_p)_l^{l-1}$ is either 1 or 0:

$$(R_p)_l^{l-1}(i,j) = \begin{cases} 1 & \text{if cell } j \text{ is inside coarser cell } i, \\ 0 & \text{otherwise.} \end{cases} \tag{19}$$

Once the grid hierarchy is established, sequential application of restriction and prolongation transforms the fine-scale FIM system into an ADM system at level l. Solving this coarser system and then prolonging the solution back to the fine grid provides an approximation to the fully resolved solution. This process significantly reduces computational costs compared to solving the original fine-scale system in all cells. The final step involves recovering the fine-scale solution $\delta\xi_f$ by iteratively applying all prolongation operators:

$$\delta\xi_f \approx \delta\xi_f' = \hat{\mathbf{P}}_f^1 \dots \hat{\mathbf{P}}_{l-1}^l \delta\xi_l^{\text{ADM}}. \tag{20}$$

3.3. Basis functions

An important element of accurate ADM simulations is constructing basis functions for pressure and overall mass fraction that can capture fine-scale geological heterogeneity. In this work, constant interpolation is used as the prolongation operator for hyperbolic variables, while multiscale basis functions [41] are employed for pressure to account for variations in transmissibility. The multiscale finite volume approach consists of two sets of overlapping coarse grids, primal and dual coarse grids, superimposed on the fine grid, as illustrated in Fig. 3. The primal coarse grid comprises N_C control volumes, denoted as Ω_i^C with $i \in \{1, \dots, N_C\}$, while the dual coarse grid consists of N_D local domains Ω_j^D. Multiscale basis functions for pressure are generated by solving a localized numerical problem defined independently within each dual coarse domain Ω_j^D.

Specifically, to localize the flow computation, a reduced boundary condition is implemented for each dual coarse domain, leading to the following localized problem formulation:

$$\begin{cases} -\nabla \cdot \left(\lambda \cdot \nabla \Phi_j^k \right) = 0 & \text{on } \Omega_j^D, \\ -\nabla_\parallel \cdot \left(\lambda \cdot \nabla \Phi_j^k \right)_\parallel = 0 & \text{on } \partial\Omega_j^D, \\ \Phi_j^k(x_i) = \delta_{ki} & \forall x_i \in \{1, \dots, N_C\}. \end{cases} \tag{21}$$
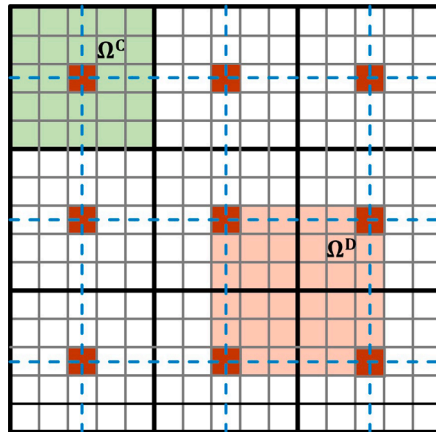
Fig. 3. Illustration of primal (bold black) and dual (dashed blue) coarse grids. Fine cells associated with a primal coarse grid (control volume) are shown in green, while those belonging to a dual coarse grid are highlighted in light orange. Coarse nodes are marked in red. (For interpretation of the references to colour in this figure legend, the reader is referred to the web version of this article.)
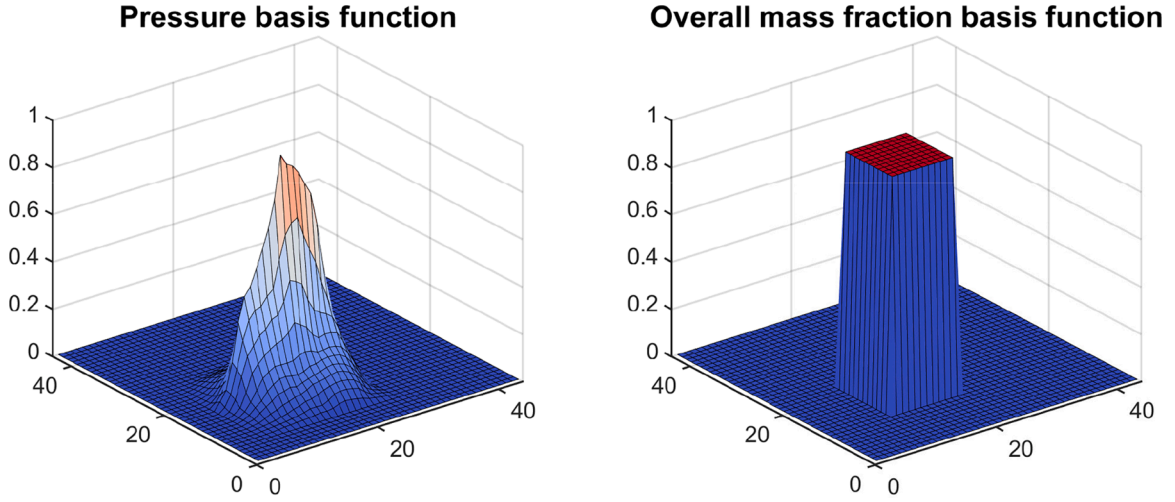
Fig. 4. Examples of multiscale and constant basis functions for pressure and overall mass fraction in a 2D heterogeneous reservoir.
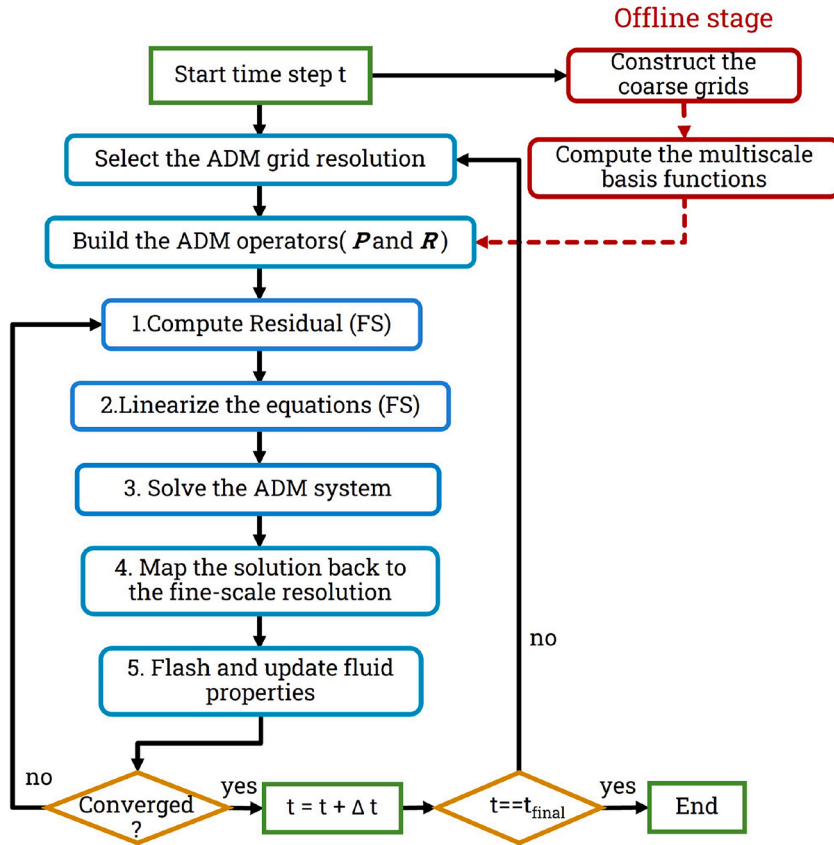

Fig. 5. Schematic overview of the ADM process for CO_2 storage in deep saline aquifers.

Here, λ is the mobility, Φ_j^k denotes the basis function associated with coarse node k in dual coarse block Ω_j^D, and δ_{ki} is the Kronecker delta. The subscript $\parallel$ indicates the only the component parallel to the boundary $\partial\Omega_j^D$ is considered. As shown in Fig. 4, a multiscale pressure basis function is generated by solving localized pressure equations within each coarse block, thereby incorporating the influence of fine-scale transmissibility contrasts.

Fig. 5 provides a schematic overview of how the ADM method is applied to CO_2 storage. Starting from a fully resolved fine grid, the solver identifies regions of steep solution gradient at each time step using a front-tracking technique and a predefined threshold.

Cells with these high gradient subdomains remain at fine resolution, along with areas near wells to preserve accuracy. Elsewhere, the domain is discretized at progressively coarser levels, forming a hierarchy of nested grids. Restriction and prolongation operators transfer unknowns and residuals between these levels, enabling an efficient coarse-scale solve before interpolating the solution back to the fine grid. A Newton linearization scheme is employed to iteratively resolve nonlinearities. With this dynamic approach, ADM naturally adapts to evolving CO_2 fronts, capturing the key plume dynamics while optimizing computational resources.

4. Numerical results

This section presents a series of numerical results, including a benchmark study, to illustrate the performance of the proposed method. We begin by validating the ADM approach on a two-dimensional synthetic model, then proceed to more complex scenarios to assess the accuracy and efficiency of our framework.

To quantify accuracy for the hyperbolic variables (i.e., x_{CO_2} and z_{CO_2}), the error metric at each time step t is defined as:

$$\epsilon_x(t) = \frac{\|x_{CO_2}(t) - x_{CO_2,f}(t)\|_1}{N_f},\tag{22}$$

where $x_{CO_2,f}$ is the fine-scale CO_2 mass fraction distribution, and N_f is the total number of fine cells at time step t. For pressure, we define:

$$\epsilon_P(t) = \frac{\sqrt{\frac{1}{N_f}\|P_w(t) - P_{w,f}(t)\|_2^2}}{P_{bc}},\tag{23}$$

where $P_{w,f}$ denotes the fine-scale wetting-phase pressure solution and P_{bc} is a characteristic pressure scale (for instance, a boundary condition value). The average errors over the entire simulation periods are computed as:

$$\epsilon_x = \text{mean}(\epsilon_x(t)),\tag{24}$$
$$\epsilon_P = \text{mean}(\epsilon_P(t)).\tag{25}$$

4.1. Test case 1: Validation of ADM

To validate the ADM method, we analyze a 2D synthetic model in the $x - z$ plane, which is specifically designed to study both convective mixing and dissolution trapping of CO_2 [42]. The domain extends $100\,m$ horizontally and $50\,m$ vertically, incorporating a static capillary transition zone (CTZ) in the upper $10\,m$. Within this CTZ, the model maintains a constant CO_2 solubility at $x_{CO_2} = 0.03$, facilitated by large pore volumes. The simulation employs fixed K-values governing the phase partitioning of CO_2 and H_2O. A small amount of water, quantified at $y_{H_2O} = 1.0 \times 10^{-4}$, vaporizes into the CO_2-rich phase, ensuring that the domain primarily consists of a single-phase brine region.

The domain is discretized into a grid of 500 by 250 cells, with each cell measuring $0.2\,m \times 0.2\,m$. A diffusion coefficient of 2×10^{-9} m^2/s applies to both components in both phases. The permeability of rock is set at 100 mD, with a porosity of 0.15. Additional model parameters are consistent with those used in [8]. For model validation, simulations are conducted using both fine-scale and ADM strategies, with the ADM model incorporating two coarse levels, each with a coarsening factor of $\gamma = 5 \times 5$. The coarsening criterion based on Δz_{CO_2} differences between neighboring cells is set at thresholds of {5e-3, 1e-3, 5e-4, 1e-4}. Both the fine-scale and ADM simulations use the same nonlinear solver tolerances, and the total simulation time is 2000 years. The initial time-step size is set to 0.1 day, and the maximum time-step size is limited to 10 days throughout the simulation.

To quantify the convective mixing, the dissolution rates are calculated, defined as the mass rate of CO_2 transitioning into the single-phase brine region:

$$F = h\phi\frac{\partial \overline{x}_{CO_2}}{\partial t},\tag{26}$$

where h and $\overline{x}_{CO_2}$ are the thickness and the average CO_2 concentration of the single-phase brine region, respectively. Fig. 6 illustrates the dissolution rate over 2000 years. Initially, there is an increase due to the formation of fingering plumes of dissolved CO_2 which propagate and enhances mass transfer. Around $t_{peel} = 350$ years, the rate transitions toward a shut-down regime, decaying with approximately a $1/t^2$ slope due to the merging of the plumes at the aquifer bottom, reducing the driving force for further dissolution. The behavior of our simulation aligns well with the previous and analytical studies.

We also evaluate the sensitivity of ADM to various refinement criteria, Δz_{CO_2}. Lower thresholds provide finer local resolution in regions with steep composition differences, enhancing the accuracy of convective flow capture. Notably, at the lowest threshold ($\Delta z = $ 1e-4), the ADM solution curve nearly overlaps with the fully resolved fine-scale reference. Conversely, higher thresholds save computational effort but may overlook some flow details.

Fig. 7 compares the CO_2 mass fraction profiles after 350 years for the fine-scale solution and the four ADM configurations, while Fig. 8 presents the error curves over time (left) and the percentage of active grid cells (AGC) in the ADM simulations (right). It is worth noting that lower Δz_{CO_2} thresholds produce closer agreement with the fine-scale solution but require more active grid cells, reflecting a trade-off between computational efficiency and model accuracy. At a threshold of 1e-3, the ADM achieves good accuracy while conserving computational resources compared to the fully resolved grid. In this case, the AGC approaches 100% after approximately 200 years, reflecting the fact that the simulation is configured to fully capture the onset and evolution of gravity-driven spreading and convective mixing processes.
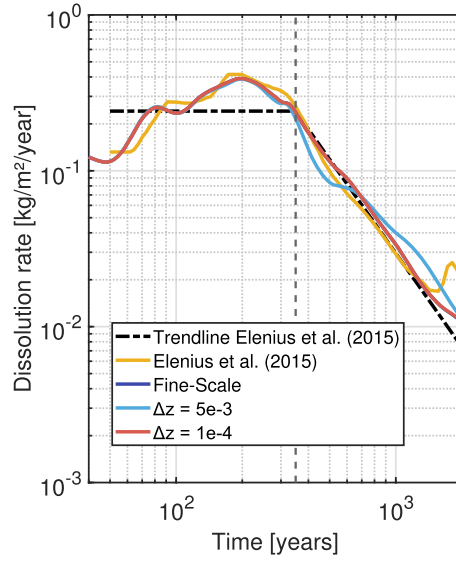
Fig. 6. Dissolution rate over 2000 years in a 100×50 m domain with a stagnant CTZ.

(a) Fine-Scale

(b) Δz = 5e-3, ε = 2.567‰, AGC = 33%

(c) Δz = 1e-3, ε = 0.413‰, AGC = 91%

(d) Δz = 5e-4, ε = 0.103‰, AGC = 99%

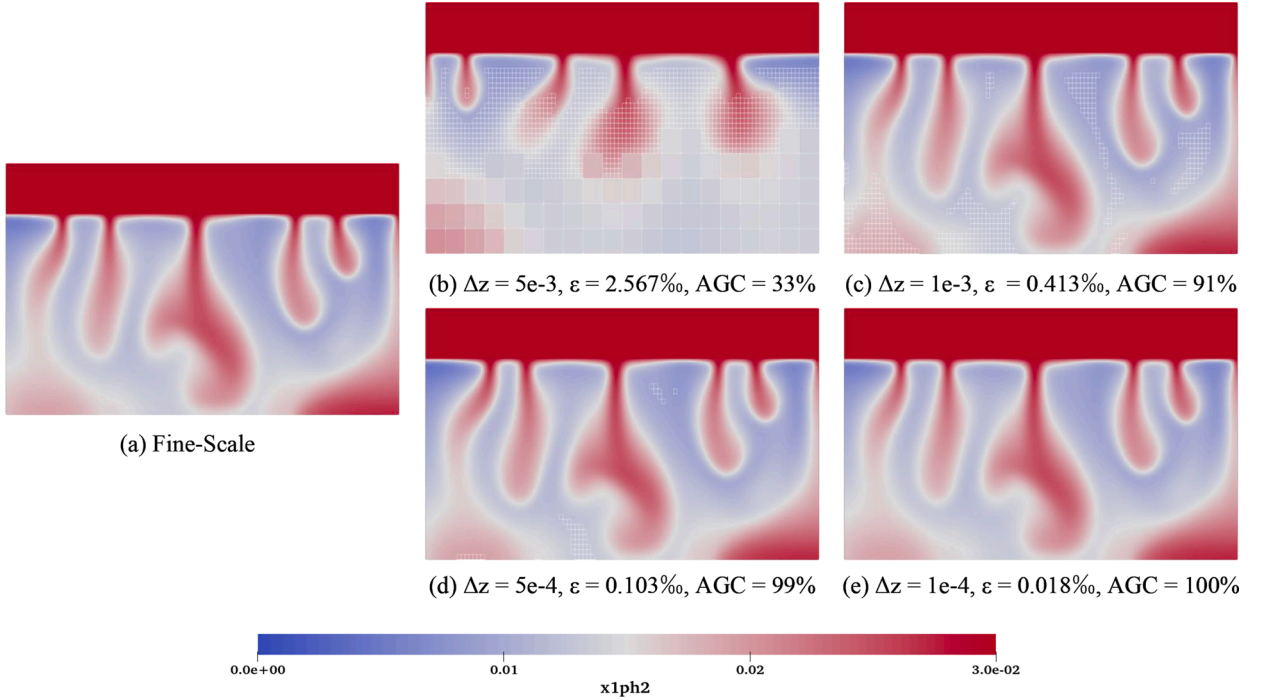(e) Δz = 1e-4, ε = 0.018‰, AGC = 100%

Fig. 7. CO_2 mass fraction profiles at 350 years. Fine-scale reference is shown alongside ADM solutions at Δz ={5e-3, 1e-3, 5e-4, 1e-4}. The overlaid grid lines show the first and second levels of coarsening.

4.2. Test case 2: Scalability evaluation in 3D aquifers

This test case investigates the scalability and efficiency of the ADM method in three-dimensional homogeneous aquifers of varying sizes. First, we consider a 100 m $\times 28$ m $\times 19$ m homogeneous reservoir with uniform porosity $\phi = 0.2$ and absolute permeability $k = 8.0 \times 10^{-14}$ m^2. Initial pressure is set at 2.5×10^7 Pa and the temperature is maintained at 65°C. The simulation setup includes an injection well at the lower-left corner with a rate of 4.0×10^{-5} pore volume per day and a production well at the upper-right corner, maintaining a bottom hole pressure of 2.5×10^7 Pa. The reservoir is discretized using a Cartesian mesh with cell dimensions of 1 m in each direction, resulting in a fine-scale grid of $100 \times 28 \times 19$ cells. For the ADM simulation, two coarse levels are employed, each with a coarsening ratio of 3 in the x, y and z directions. A coarsening criterion of 0.01 is used, indicating that cells exceeding this
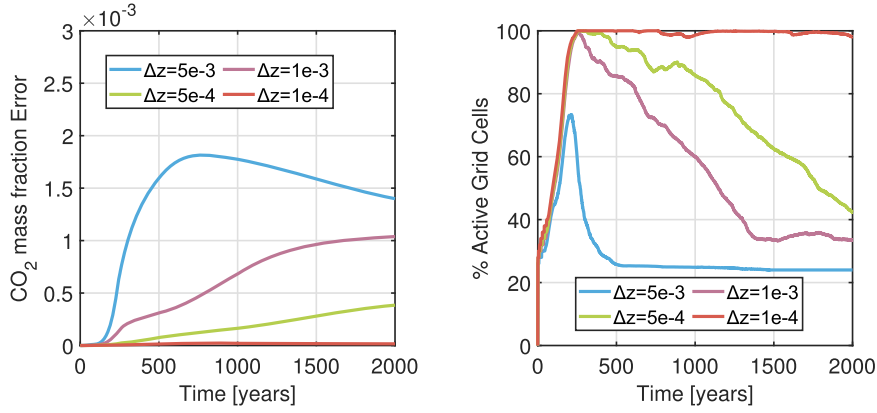
Fig. 8. CO_2 mass fraction errors (left) and percentage of active grid cells (right) over time for different threshold settings, illustrating the precision-efficiency balance.
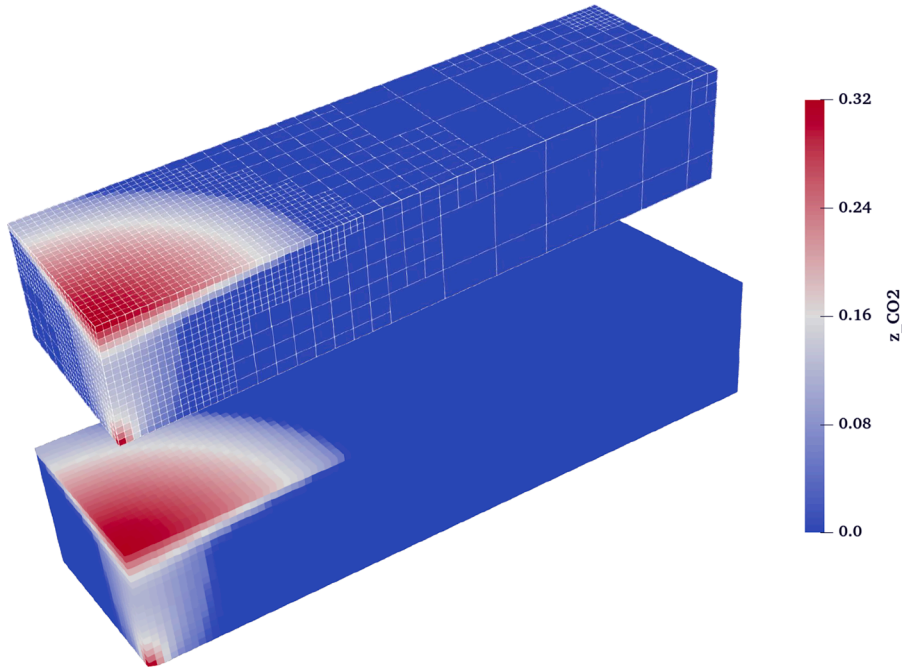

Fig. 9. Comparative visualization of overall CO_2 mass fraction profiles between ADM (top) and the fine-scale model (bottom) after 200 days.

threshold in z_{CO_2} gradient remain refined to capture significant changes accurately. The initial time-step size is set to 0.01 day, and the maximum time-step size is limited to 5 days.

The CO_2 distribution predicted by ADM closely matches that of the fine-scale reference after 200 days, as illustrated in Fig. 9. The figure highlights the coarse-to-fine transition of grid cells in regions of significant overall CO_2 mass fraction changes, while other areas are coarsened without compromising the accuracy of the simulation. Indeed, error calculations using Eq. 22 show a difference of only 1.5×10^{-6}, demonstrating ADM's effectiveness at reducing computational effort while preserving key flow characteristics.

To further explore the influence of problem size on the ADM algorithm, three homogeneous reservoirs of different dimensions are considered: $100\,m \times 28\,m \times 19\,m$, $199\,m \times 55\,m \times 19\,m$ and $397\,m \times 109\,m \times 19\,m$. Each model is discretized with $\Delta x = \Delta y = \Delta z = 1\,m$, and the same permeability, porosity and well configuration are applied. The injection rates are adjusted relative to pore volume, with each simulation extending over 5000 days, including 600 days of injection followed by 4400 days of post-injection monitoring.

Fig. 10 compares the evolution of active grid cell percentages over the simulation period across varying problem sizes. The results show that ADM efficiency improves with larger domains, especially when injection impacts only a limited reservoir portion. This allows extensive grid coarsening, significantly reducing computational resources needed for long-duration and large-scale simulations. These results highlight ADM's adeptness at dynamically refine critical areas and efficiently coarsen non-critical regions, demonstrating its improved effectiveness in large-scale operations.
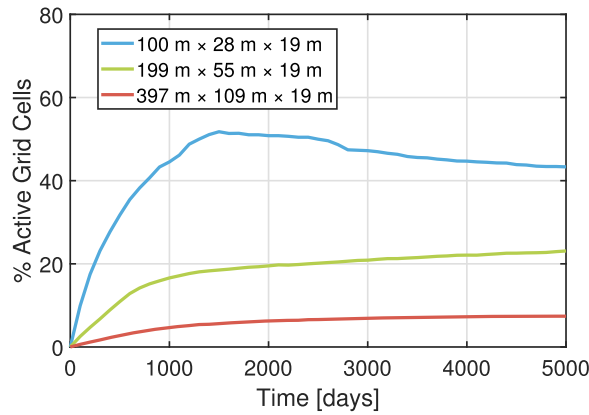
Fig. 10. Evolution of active grid cell percentages employed by ADM during simulation with the threshold value of 0.01.
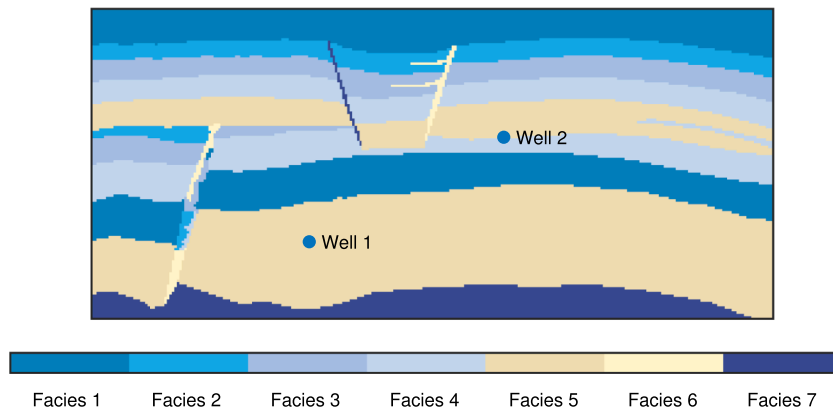

Fig. 11. Illustration of the discretized two-dimensional geometry of the SPE 11A model, showcasing the arrangement of facies and injection wells locations.

4.3. Test case 3: SPE 11A at laboratory conditions

Further validation of the ADM framework is conducted through its application to the SPE 11A benchmark model, designed to simulate CO_2 storage under controlled laboratory conditions [36]. This model, which mimics the downscaled characteristics of North Sea storage formations, features a two-dimensional representation encompassing seven distinct facies. These include one seal, five permeable reservoir sands, and one impermeable layer, all inspired by extensive laboratory experiments and illustrated in Fig. 11. The properties of these unconsolidated sands are consistent with recent studies from [43], as summarized in Table 1.

The domain geometry measures $2.8\,\text{m}$ in length and $1.2\,\text{m}$ in height, with a uniform thickness of $0.01\,\text{m}$. The domain is discretized into a grid of 280×127 cells, yielding a total of 35560 control volumes. The isothermal conditions are maintained at 20 °C, corresponding to atmospheric pressure. The left, right, and bottom boundaries are treated as no-flow boundaries, while the top boundary is maintained at a constant pressure of 1.1×10^5 Pa and is in direct contact with pure water. The initial time-step size is set to 10^{-6} minute, and the maximum time-step size is limited to 10 min throughout the simulation. The simulation monitors CO_2 flow and transport over a total duration of 5 days. Initially, the medium is saturated with water, and CO_2 is injected through two injection wells,

Table 1
Physical parameters and simulation setup for the SPE 11A numerical simulation.

	k [D]	ϕ [-]	S_{wi} [-]	P_{entry} [Pa]	D_w [m²s⁻¹]	D_n [m²s⁻¹]
Facies 1	44.53	0.44	0.32	1500	10^{-9}	1.6×10⁻⁵
Facies 2	506.63	0.43	0.14	300	10^{-9}	1.6×10⁻⁵
Facies 3	1013.25	0.44	0.12	100	10^{-9}	1.6×10⁻⁵
Facies 4	2026.50	0.45	0.12	25	10^{-9}	1.6×10⁻⁵
Facies 5	4953.00	0.43	0.12	10	10^{-9}	1.6×10⁻⁵
Facies 6	10132.50	0.46	0.10	1	10^{-9}	1.6×10⁻⁵
Facies 7	10^{-8}	10^{-5}	0	0	0	0

as shown in Fig. 11. The first well operates continuously for the initial 5 h, injecting CO_2 at a rate of 1.7×10^{-7} kg/s. Subsequently, the second well begins injection at 2.5 h, and continues until 5 h, maintaining the same injection rate and thereby overlapping with the first well for half the duration. This setup facilitates detailed observation of CO_2 distribution and phase interactions within the porous medium.

Relative permeability and capillary pressure curves are modeled using the Brooks-Corey equations, adapted to each sand type according to their respective residual saturation values. Specifically, the relative permeability k_r is given by:

$$k_{r,\alpha} = \left(\max\left(\frac{S_\alpha - S_{\alpha,\text{imm}}}{1 - S_{\alpha,\text{imm}}}, 0 \right) \right)^2, \tag{27}$$

where $S_{\alpha,\text{imm}}$ is the residual saturation of phase α, below which the phase becomes immobile. A residual saturation of 0.1 is specified for the non-wetting phase across all facies. The extended Brooks-Corey function for all saturations is:

$$P_c = P_{c,\text{max}} \cdot \text{erf}\left(\frac{P_{\text{entry}} \cdot (S_{w,n})^{-\frac{1}{2}}}{P_{c,\text{max}}} \cdot \frac{\sqrt{\pi}}{2} \right), \tag{28}$$

where $S_{w,n}$ is the normalized wetting-phase saturation, P_{entry} denotes the rock entry pressure, and $P_{c,\text{max}} = 2500$ Pa specifies the maximum capillary pressure. The thermophysical properties of pure CO_2 and H_2O phases are obtained from the NIST database [44].

To optimize computational resources, the ADM simulations are conducted with two coarse levels, and the coarsening ratio is $\gamma = 3 \times 3$. We explore four different thresholds {5e-3, 1e-3, 5e-4, 1e-4} for the coarsening criterion based on Δz_{CO_2}. Over the full-cycle period, including both injection and post-injection phase, the system captures CO_2 plume evolution, dissolution, and convective transport.

Fig. 12 displays CO_2 mass fraction profiles after five hours of injection, comparing the fine-scale baseline with various coarsening thresholds. The illustration highlights the rapid upward and lateral movement of CO_2 driven by buoyancy forces and its interaction with the sealing layer. This visualization demonstrates the effectiveness of the ADM in capturing the early stages of CO_2 plume development under dynamic storage conditions. Fig. 13, on the other hand, presents the CO_2 distribution after five days, illustrating the post-injection phase, during which the CO_2-saturated upper layer, denser than the underlying brine, begins to form descending fingers at the interface. These structures indicate the onset of gravitational instability, a critical factor for understanding long-term CO_2 storage efficiency. Although the fine-scale simulation offers a comprehensive understanding of these dynamics, the ADM simulations achieve high accuracy throughout the injection period, with minor errors. During the post-injection phase, reducing the coarsening threshold from $\Delta z_{CO_2} = 1\text{e-}3$ to $\Delta z_{CO_2} = 5\text{e-}4$ results in only a slight increase in the active grid cells but enhances accuracy. The most refined ADM configuration, with $\Delta z_{CO_2} = 1\text{e-}4$, achieves the lowest error and highest AGC, effectively replicating the fine-scale model's complex dynamics and enabling precise visualization of individual finger migrations.

The capability of ADM to effectively track these complex features using fewer active grid cells is quantitatively analyzed in Fig. 14. Fig. 14(a) and (b) present the ADM error metrics for pressure and overall mass fraction, respectively, throughout the simulation duration. Fig. 14(c) details the percentage of active grid cells utilized by ADM and Fig. 14(d) summarizes the average errors and active
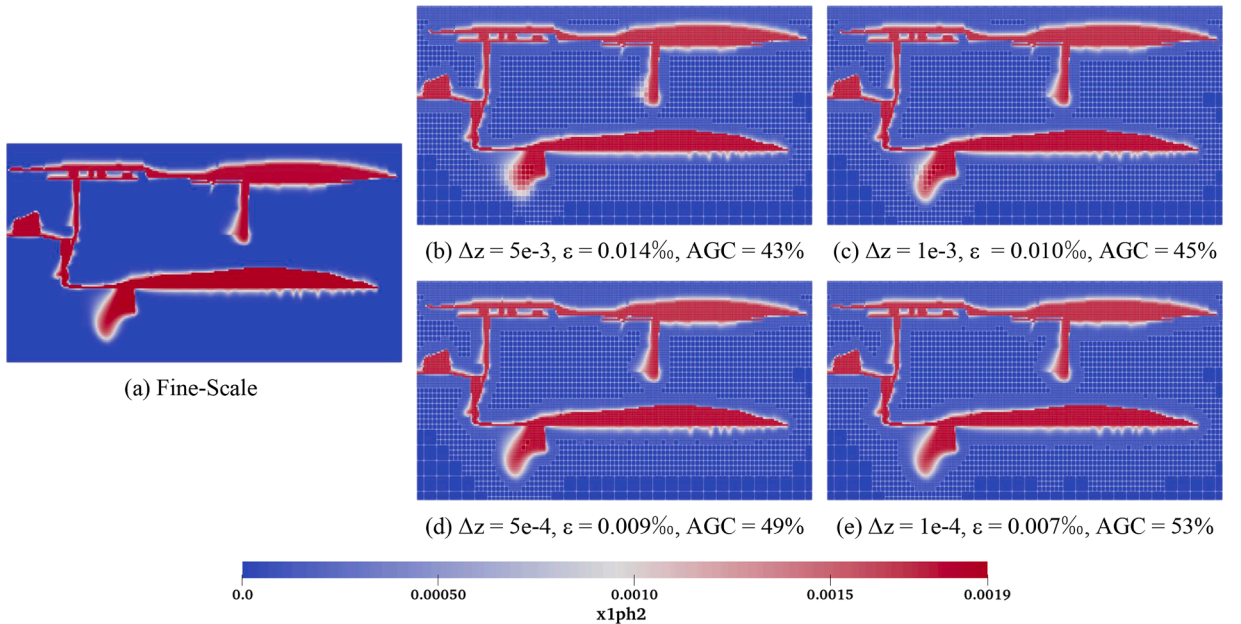

(a) Fine-Scale

(b) $\Delta z = 5\text{e-}3$, $\varepsilon = 0.014‰$, AGC $= 43\%$　　(c) $\Delta z = 1\text{e-}3$, $\varepsilon = 0.010‰$, AGC $= 45\%$

(d) $\Delta z = 5\text{e-}4$, $\varepsilon = 0.009‰$, AGC $= 49\%$　　(e) $\Delta z = 1\text{e-}4$, $\varepsilon = 0.007‰$, AGC $= 53\%$

0.0　　　　0.00050　　　　0.0010　　　　0.0015　　　　0.0019
x1ph2

Fig. 12. CO_2 mass fraction profiles for SPE 11A model after 5 h injection, showing the finest and coarse grid levels.
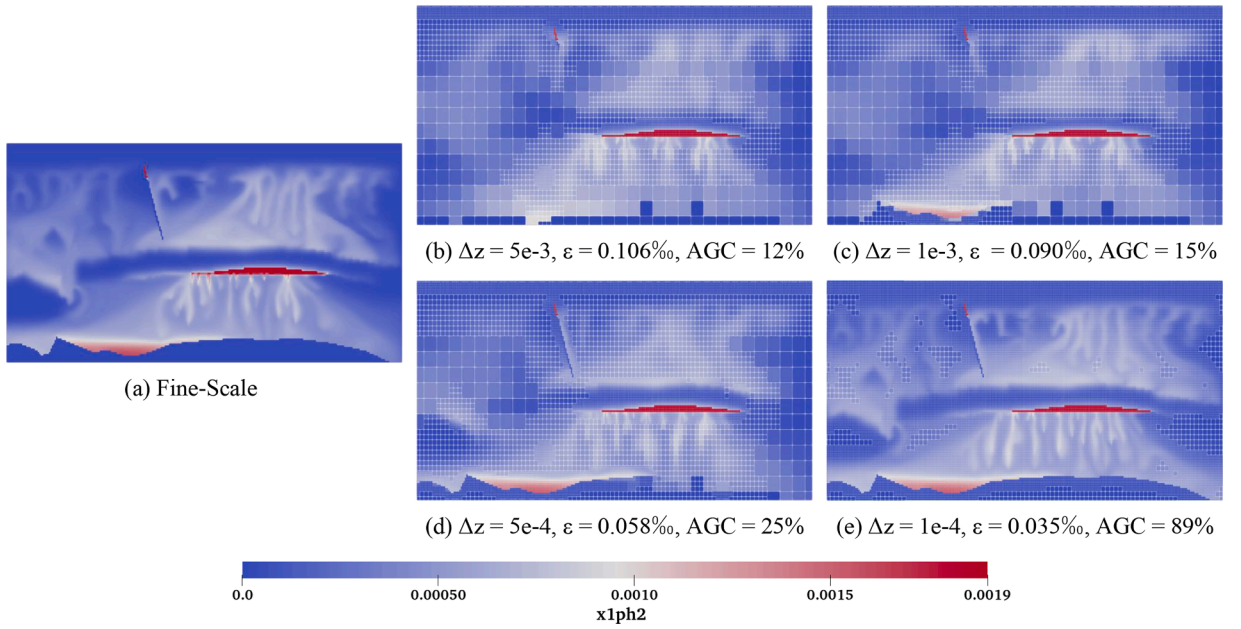
Fig. 13. CO_2 mass fraction profiles for SPE 11A model after 5 days, illustrating detailed plume behavior across fine and coarse grid levels.

cell fractions across all thresholds. This analysis confirms that tighter thresholds, such as 1e-4, result in lower errors but require a higher number of active cells, highlighting a trade-off between precision and efficiency. Lastly, Fig. 15 depicts the fractions of injected CO_2 that remain mobile and that dissolves into the brine over the simulation duration. During injection, most of the CO_2 remains in the mobile phase. Afterward, dissolution and reactivation due to convective transport triggered by density gradients, reactivate a portion of the mobile gas. All ADM configurations closely match the fine-scale reference, indicating that resolving individual fingers in detail is not strictly necessary to accurately capture overall trapping dynamics.

4.4. Test case 4: SPE 11B at reservoir conditions

Building on the methodologies validated in the laboratory-scale SPE 11A setup, the SPE 11B benchmark extends the simulations to mimic reservoir conditions characteristic of the Norwegian Continental Shelf. While retaining the basic geometric framework of SPE 11A, SPE 11B scales up the model to field dimensions. Specifically, the horizontal dimensions are scaled by a factor of 1:3000 and the vertical dimensions by 1:1000, resulting in a large-scale model measuring $8.4\,km$ in length and $1.2\,km$ in height. Well placements are adjusted accordingly, as shown in Fig. 16. The model assumes a uniform thickness of $1\,m$. To accurately reflect reservoir conditions, the facies properties are updated, with details provided in Table 2.

While the official SPE 11B benchmark considers thermal effects, this study maintains a focus on mass conservation equations due to the scope of our research. The domain is discretized into a grid of 847×127. The temperature is uniformly maintained at 50 °C throughout the simulation. Initially the domain is fully saturated with water, and CO_2 is injected through two injection wells. The first well operates at a constant injection rate of $0.035\,kg/s$ for 50 years. A second well begins injection at the same rate after 25 years, resulting in a 25-year period of overlapping operation. The initial time-step size is set to 1 minute, and the maximum time-step size is limited to 36.5 days throughout the simulation. These simulation setups are crucial for monitoring the long-term migration of the CO_2 plume under these extended temporal and spatial scales.

To prevent unphysical pressure buildup, auxiliary porosity volumes are introduced along the lateral boundaries, facilitating pressure stabilization across the field as detailed in referenced studies [36]. Moreover, permeability is assigned using an anisotropy ratio of 10:1 between horizontal and vertical directions ($k_z = 0.1k_h$). Differences from SPE 11A include adjustments in capillary pressures, which are defined according to the Leverett J-scaling:

$$P_{entry} = \sqrt{\frac{\phi}{k_x}} \cdot 6.12 \times 10^{-3} \text{N/m}. \tag{29}$$

where 6.12×10^{-3} N/m is derived from [45]. Additionally, shape exponents for relative permeability and capillary forces are adjusted to 1.5, with respective curves for each facies shown in Fig. 17. The thermodynamic parameters remain consistent with those defined in the SPE 11A model, ensuring physical consistency in the simulation's physical modeling across different test cases. This comprehensive setup allows for an extensive analysis of CO_2 behavior under reservoir conditions, providing valuable insights into its long-term migration patterns.
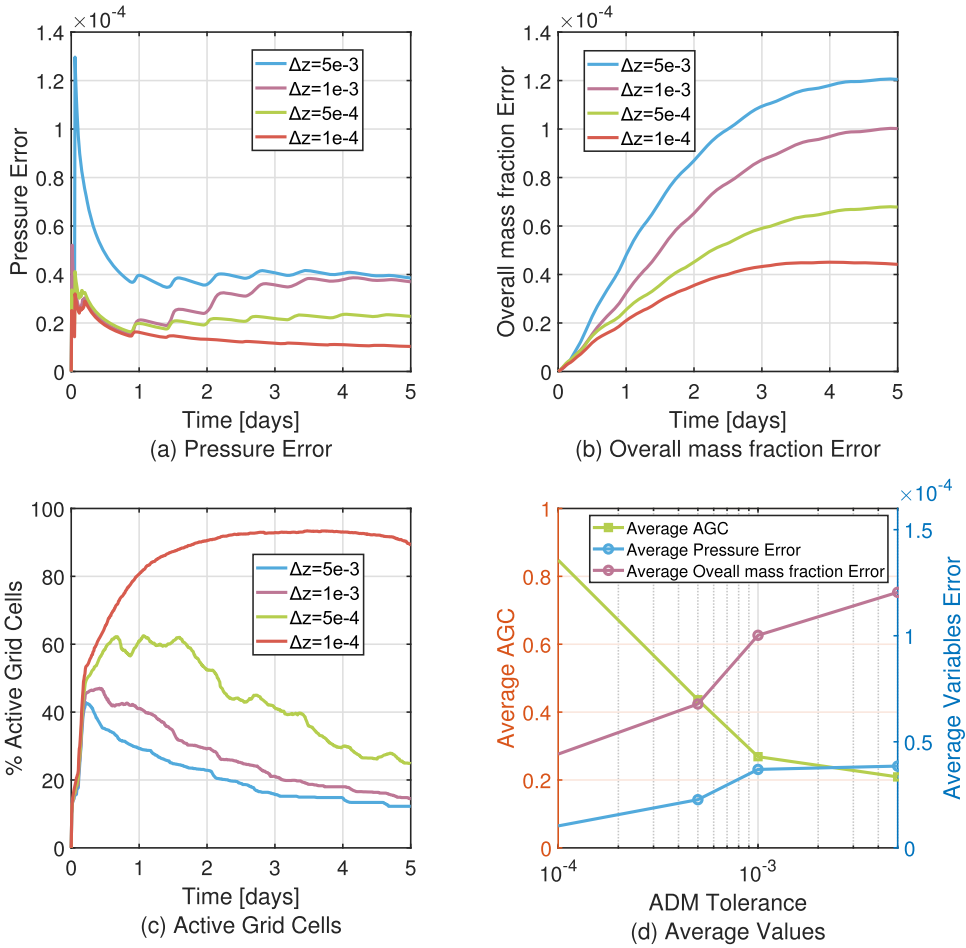
Fig. 14. SPE 11A error analysis detailing ADM performance across various thresholds, with metrics for pressure, mass fraction errors, and active grid cell usage.
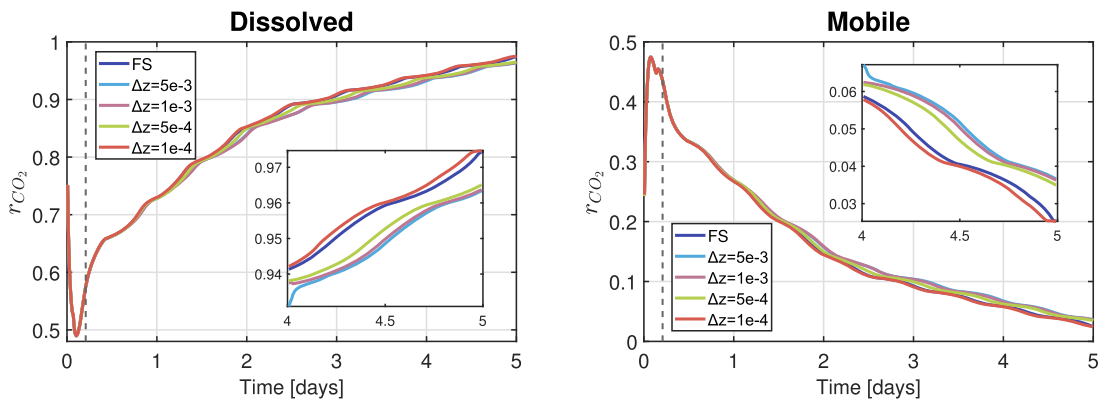

Fig. 15. Temporal dynamics of CO_2 trapping in the SPE 11A model, illustrated as fractions of injected CO_2 in dissolved and mobile states. The vertical dashed line indicates the transition moment at which injection stops.

Fig. 18 presents the comparative results at the end of the injection phase, utilizing both the ADM method and a fine-scale reference model. The simulations explore varying coarsening thresholds of $\Delta z_{CO_2} \in \{0.1, 0.05, 0.01, 0.001\}$, with a consistent coarsening ratio of $\gamma = 3 \times 3$. In all models, the CO_2 plume rises vertically due to buoyancy, subsequently spreading laterally at sealing layers, illustrating the complex interactions of the plume with geological structures. The fine-scale model provides a baseline for assessing the impact of ADM's varied coarse levels on simulation accuracy. During the initial injection phase, discrepancies between the ADM simulations
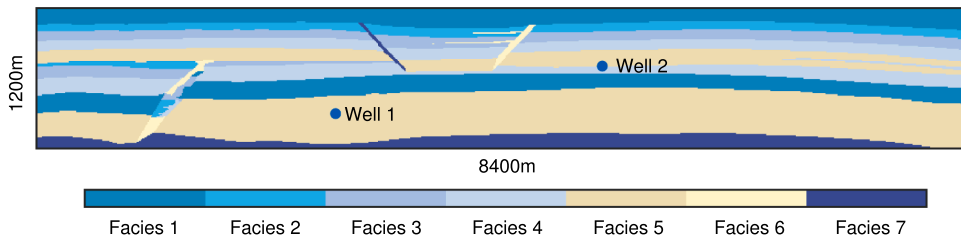
Fig. 16. Illustration of the SPE 11B model geometry, showing scaled dimensions and well placements in a field scenario.

Table 2
Physical parameters and simulation setup for the SPE 11B numerical simulation.

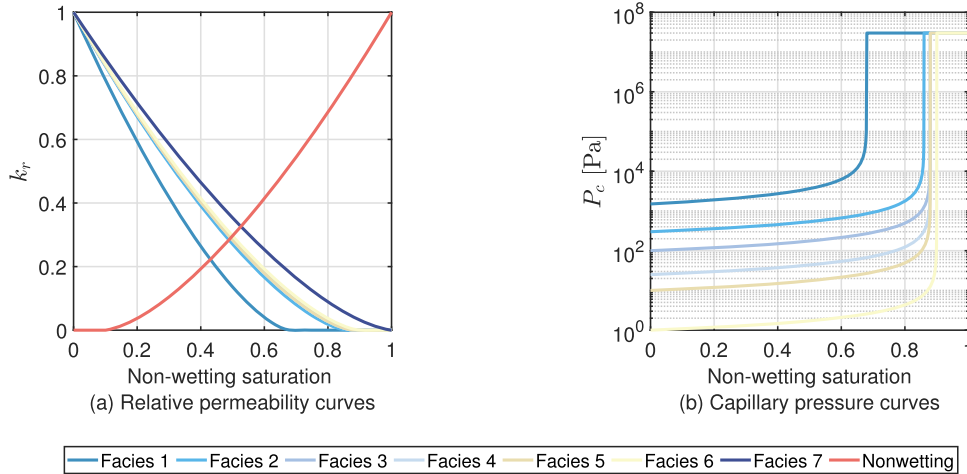|	k_h [mD]	ϕ [-]	S_{wi} [-]	D_w [m^{2}s^{-1}]	D_n [m^{2}s^{-1}]
Facies 1	0.10132	0.10	0.32	10^{-9}	2×10^{-8}
Facies 2	101.324	0.20	0.14	10^{-9}	2×10^{-8}
Facies 3	202.65	0.20	0.12	10^{-9}	2×10^{-8}
Facies 4	506.625	0.20	0.12	10^{-9}	2×10^{-8}
Facies 5	1013.25	0.25	0.12	10^{-9}	2×10^{-8}
Facies 6	2026.5	0.35	0.10	10^{-9}	2×10^{-8}
Facies 7	10^{-5}	10^{-5}	0	0	0

Fig. 17. Relative permeability and capillary pressure curves for different sand facies as a function of non-wetting saturation.

remain minimal, largely because the CO_2 plume impacts only a small section of the domain, allowing for a coarser grid in the majority of the domain.

Fig. 19 displays the long-term CO_2 distribution after 1000 years, highlighting the divergence in simulation accuracy across different coarsening thresholds. As the coarsening threshold decreases from $\Delta z = 0.1$ to $\Delta z = 0.001$, the ADM simulations progressively capture the plume dynamics with increased precision. The lower thresholds, particularly in Fig. 19(d) and (e), reveal more intricate fingering patterns of CO_2 migration, aligning more closely with those observed in the fine-scale model.

Moreover, Fig. 20 presents a comprehensive error analysis for SPE 11B simulations across different ADM coarsening thresholds, illustrating how adjustments in Δz impact the accuracy and computational efficiency of the model over a 1000-year simulation period. Fig. 20(b) depicts the overall mass fraction error, which reveals a distinct trend. Lower Δz values correspond to lower errors, demonstrating improved mass fraction accuracy with finer grid resolutions. This improvement becomes more pronounced over time, underscoring the ADM method's capability to capture detailed physics interactions within the CO_2 plume more effectively as the grid resolution increases. Simultaneously, as Δz decreases, the percentage of active grid cells increases, peaking significantly for the finest threshold ($\Delta z = 0.001$), which reflects the method's dynamic grid adaptation to the evolving simulation demands, particularly in capturing finer details of plume behavior. Fig. 20(d) integrates these metrics, correlating the average active grid cells, average pressure error, and average overall mass fraction error against the ADM tolerance thresholds, highlighting the trade-offs between computational cost and simulation accuracy.

Lastly, Fig. 21 shows that varying ADM coarsening thresholds has only a minor impact on the quantification of CO_2 in both dissolved and mobile phases over the 1000-year simulation. This suggests that, even with broader coarsening thresholds, the ADM
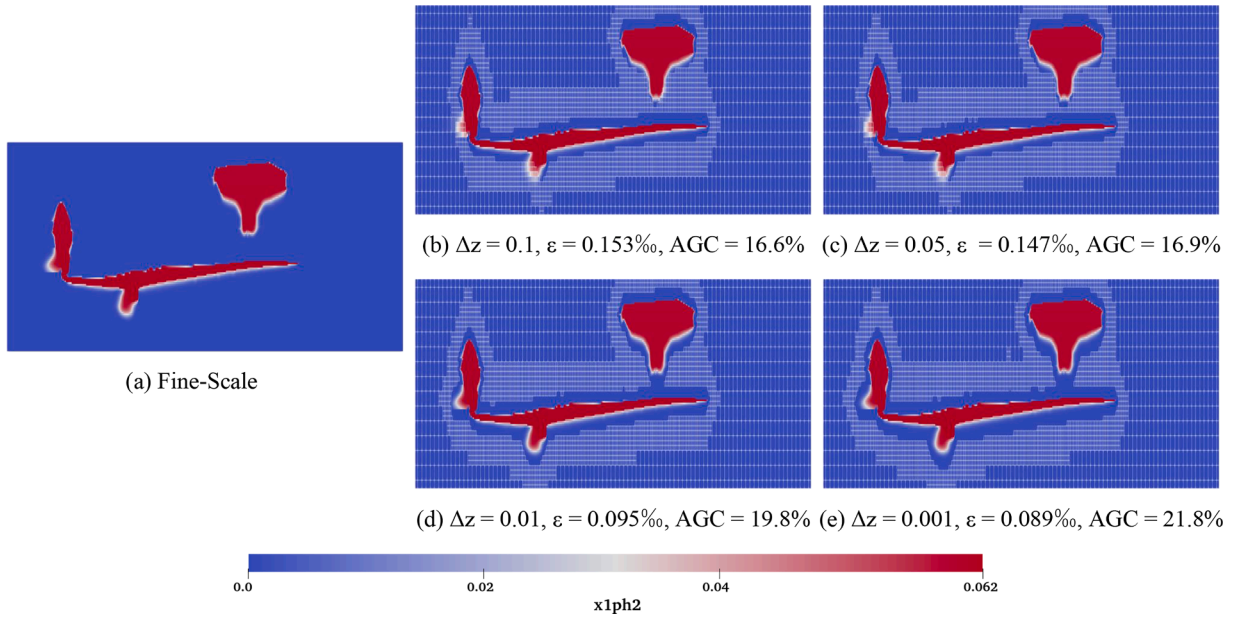
(b) $\Delta z = 0.1$, $\varepsilon = 0.153‰$, AGC = 16.6%   (c) $\Delta z = 0.05$, $\varepsilon = 0.147‰$, AGC = 16.9%

(a) Fine-Scale

(d) $\Delta z = 0.01$, $\varepsilon = 0.095‰$, AGC = 19.8%   (e) $\Delta z = 0.001$, $\varepsilon = 0.089‰$, AGC = 21.8%

Fig. 18. CO_2 mass fraction profiles for SPE 11B model after 50 years injection. The overlaid grids represent the first and second levels of coarsening used in the ADM simulations.
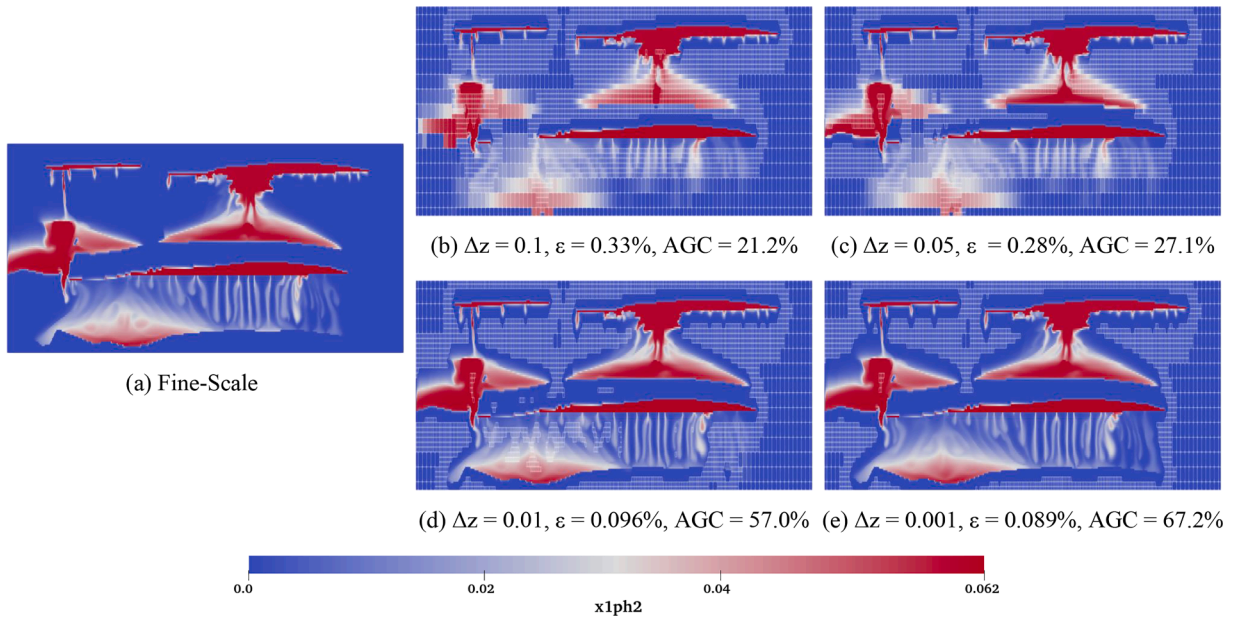

(b) $\Delta z = 0.1$, $\varepsilon = 0.33%$, AGC = 21.2%   (c) $\Delta z = 0.05$, $\varepsilon = 0.28%$, AGC = 27.1%

(a) Fine-Scale

(d) $\Delta z = 0.01$, $\varepsilon = 0.096%$, AGC = 57.0%   (e) $\Delta z = 0.001$, $\varepsilon = 0.089%$, AGC = 67.2%

Fig. 19. CO_2 mass fraction profiles for SPE 11B model after 1000 years. The overlaid grids represent the first and second levels of coarsening used in the ADM simulations.

method still effectively captures the essential dynamics of CO_2 trapping mechanisms in deep saline aquifers. The fractional amounts of injected CO_2 in both dissolved and mobile phases follow similar trajectories across different thresholds, indicating robustness in the ADM's ability to model long-term behavior regardless of the grid coarseness. Even with relatively larger thresholds, the method provides a rapid and efficient quantification approach without significantly compromising the accuracy, making it suitable for extensive parameter studies or scenarios with limited computational resources.

Overall, these findings confirm that the ADM approach validated against fine-scale models retains its ability to capture key CO_2 transport phenomena, including dissolution-driven density changes and extended migration patterns.
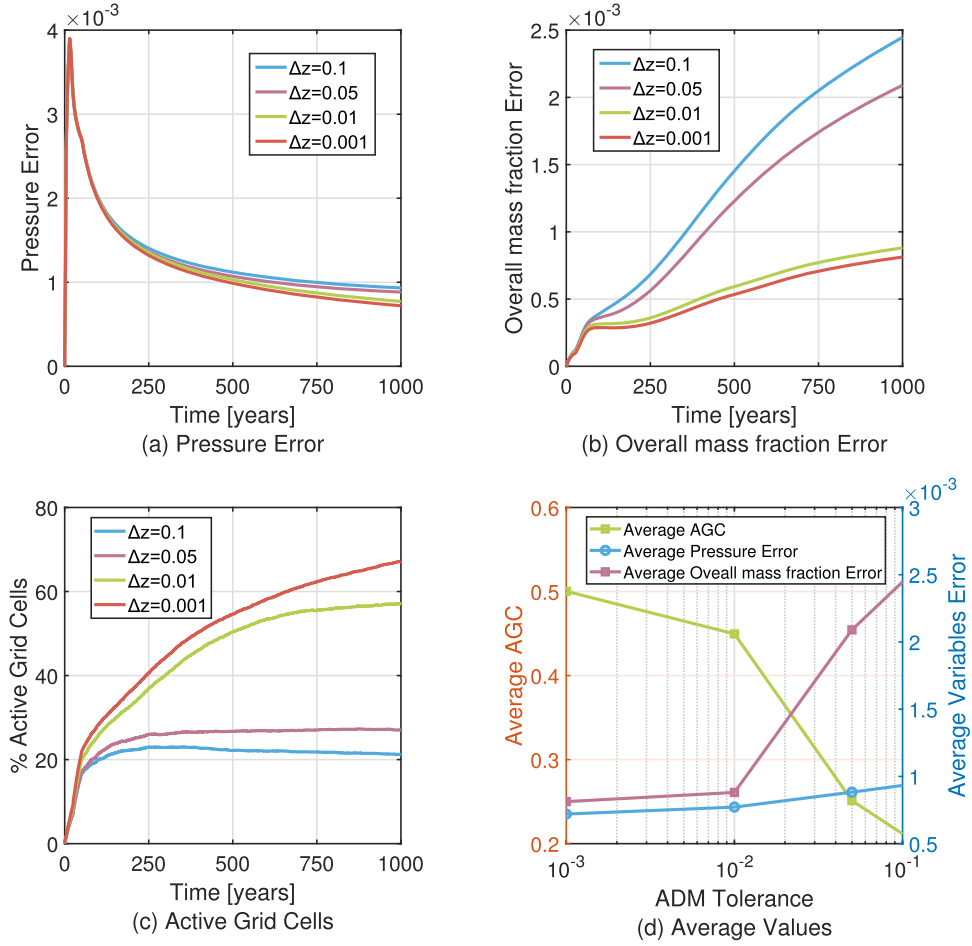
Fig. 20. Error analysis for the SPE 11B ADM simulations, showing variations in pressure and mass fraction errors alongside the percentage of active grid cells used across different coarsening thresholds.
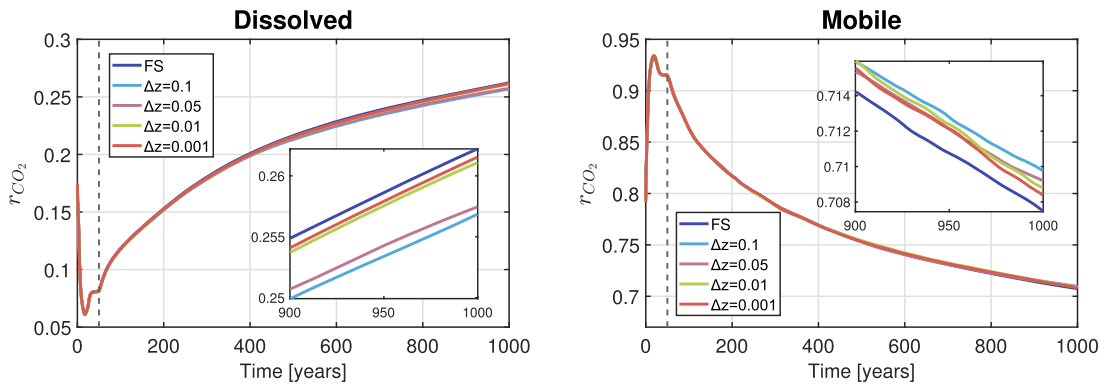

Fig. 21. Temporal dynamics of CO_2 trapping in the SPE 11B model, illustrated as fractions of injected CO_2 in dissolved and mobile states. The vertical dashed line indicates the transition moment at which injection stops.

5. Conclusions

This study comprehensively explored the dynamics of CO_2 storage in deep saline aquifers, employing both laboratory and field-scale models to validate the effectiveness of the Algebraic Dynamic Multilevel (ADM) method. This method, characterized by its fully implicit scheme, integration of fully compositional thermodynamics, and dynamic mesh refinement based on localized over-

all CO_2 mass fraction gradients, adeptly manages various reservoir scales, rock properties, and simulation time frames. The ADM method has consistently demonstrated the ability to accurately simulate the complex interactions and flow behaviors of multiphase, multicomponent CO_2-brine systems, all while utilizing considerably fewer active grid cells than fully resolved grid approaches. By finely tuning the coarsening thresholds, the method strikes an optimal balance between computational efficiency and accuracy of the solution. Lower thresholds enable detailed capture of fine-scale fingering phenomena with increased computational demands due to enhanced grid resolution. Conversely, slightly higher thresholds manage to conserve computational resources without substantially sacrificing key flow and dissolution characteristics, as even a partial resolution of individual fingers and interfaces can be adequate to accurately replicate overall trapping dynamics. From a CCS perspective, the results demonstrate that ADM-based simulations can reliably forecast plume evolution, trapping dynamics, and dissolution processes without the excessive computational costs associated with uniformly fine grids. This capability is pivotal for devising effective CO_2 injection strategies and for the long-term assessment of CO_2 sequestration viability in geologically diverse and heterogeneous aquifer systems. The insights garnered from this study underscore the potential of ADM to facilitate more efficient and scalable simulations, making it an invaluable tool in the ongoing efforts to enhance the predictability and effectiveness of CCS technologies.

CRediT authorship contribution statement

Mengjie Zhao: Writing – original draft, Visualization, Validation, Methodology, Conceptualization; **Marc Gerritsma:** Writing – review & editing, Supervision, Methodology, Conceptualization; **Mohammed Al Kobaisi:** Software, Methodology, Conceptualization; **Hadi Hajibeygi:** Writing – review & editing, Supervision, Methodology, Funding acquisition, Conceptualization.

Data availability

Data will be made available on request.

Declaration of competing interest

The authors declare that they have no known competing financial interests or personal relationships that could have appeared to influence the work reported in this paper.

Acknowledgements

References

[1] M.E. Boot-Handford, J.C. Abanades, E.J. Anthony, M.J. Blunt, S. Brandani, N. Mac Dowell, J.R. Fernández, M.-C. Ferrari, R. Gross, J.P. Hallett, et al., Carbon capture and storage update, Energy & Environ. Sci. 7 (1) (2014) 130–189.

[2] M. Bui, C.S. Adjiman, A. Bardow, E.J. Anthony, A. Boston, S. Brown, P.S. Fennell, S. Fuss, A. Galindo, L.A. Hackett, et al., Carbon capture and storage (CCS): the way forward, Energy & Environ. Sci. 11 (5) (2018) 1062–1176.

[3] Z. Li, M. Dong, S. Li, S. Huang, CO_2 Sequestration in depleted oil and gas reservoirs–caprock characterization and storage capacity, Energy Convers. Manage. 47 (11-12) (2006) 1372–1382.

[4] S. Krevor, H. De Coninck, S.E. Gasda, N.S. Ghaleigh, V. de Gooyert, H. Hajibeygi, R. Juanes, J. Neufeld, J.J. Roberts, F. Swennenhuis, Subsurface carbon dioxide and hydrogen storage for a sustainable energy future, Nature Rev. Earth & Environ. 4 (2) (2023) 102–118.

[5] E. Lindeberg, D. Wessel-Berg, Vertical convection in an aquifer column under a gas cap of CO_2, Energy Convers. Manage. 38 (1997) S229–S234.

[6] J. Ennis-King, L. Paterson, Role of convective mixing in the long-term storage of carbon dioxide in deep saline formations, in: SPE Annual Technical Conference and Exhibition, SPE, 2003, pp. SPE–84344.

[7] K. Michael, A. Golab, V. Shulakova, J. Ennis-King, G. Allinson, S. Sharma, T. Aiken, Geological storage of CO_2 in saline aquifers–a review of the experience from existing storage operations, Int. J. Greenhouse Gas Control 4 (4) (2010) 659–667.

[8] M.T. Elenius, D.V. Voskov, H.A. Tchelepi, Interactions between gravity currents and convective dissolution, Adv. Water Resour. 83 (2015) 77–88.

[9] L. Nghiem, V. Shrivastava, B. Kohse, M. Hassam, C. Yang, Simulation and optimization of trapping processes for CO_2 storage in saline aquifers, J. Can. Pet. Technol. 49 (08) (2010) 15–22.

[10] A. Mazzoldi, T. Hill, J.J. Colls, Assessing the risk for CO_2 transportation within CCS projects, CFD modelling, Int. J. Greenhouse Gas Control 5 (4) (2011) 816–825.

[11] H. Hajibeygi, G. Bonfigli, M.A. Hesse, P. Jenny, Iterative multiscale finite-volume method, J. Comput. Phys. 227 (19) (2008) 8604–8621.

[12] M. Liu, D. Grana, Petrophysical characterization of deep saline aquifers for CO_2 storage using ensemble smoother and deep convolutional autoencoder, Adv. Water Resour. 142 (2020) 103634.

[13] M. Zhao, Y. Wang, M. Gerritsma, H. Hajibeygi, A physics-constraint neural network for CO_2 storage in deep saline aquifers during injection and post-injection periods, Adv. Water Resour. 193 (2024) 104837.

[14] X. Jiang, A review of physical modelling and numerical simulation of long-term geological storage of CO_2, Appl. Energy 88 (11) (2011) 3557–3566.

[15] B. Flemisch, J.M. Nordbotten, M. Fernø, R. Juanes, J.W. Both, H. Class, M. Delshad, F. Doster, J. Ennis-King, J. Franc, et al., The FluidFlower validation benchmark study for the storage of CO_2, Transp. Porous Media 151 (5) (2024) 865–912.

[16] H.K. Versteeg, W. Malalasekera, Computational fluid dynamics: the finite volume method, Harlow, England: Longman Scient. & Techn. (1995).

[17] J.N. Reddy, An introduction to the finite element method, New York 27 (14) (1993).

[18] Y. Wang, T.H. Chakrapani, Z. Wen, H. Hajibeygi, Pore-scale simulation of H_2-brine system relevant for underground hydrogen storage: a lattice Boltzmann investigation, Adv. Water Resour. (2024) 104756.

[19] Y. Wang, C. Vuik, H. Hajibeygi, Analysis of hydrodynamic trapping interactions during full-cycle injection and migration of CO_2 in deep saline aquifers, Adv. Water Resour. 159 (2022) 104073.

[20] Y. Wang, C. Vuik, H. Hajibeygi, CO_2 Storage in deep saline aquifers: impacts of fractures on hydrodynamic trapping, Int. J. Greenhouse Gas Control 113 (2022) 103552.

[21] K. Kala, D. Voskov, Element balance formulation in reactive compositional flow and transport with parameterization technique, Comput. Geosci. 24 (2) (2020) 609–624.

[22] E. Ahusborde, B. Amaziane, M.I. Moulay, High performance computing of 3D reactive multiphase flow in porous media: application to geological storage of CO_2, Comput. Geosci. 25 (6) (2021) 2131–2147.

[23] X. Lyu, D. Voskov, Advanced modeling of enhanced CO_2 dissolution trapping in saline aquifers, Int. J. Greenhouse Gas Control 127 (2023) 103907.

[24] R. Iskhakov, High-resolution numerical simulation of CO_2 sequestration in saline aquifers, Ph.D. thesis, Stanford University, 2014.

[25] T. Praditia, R. Helmig, H. Hajibeygi, Multiscale formulation for coupled flow-heat equations arising from single-phase flow in fractured geothermal reservoirs, Comput. Geosci. 22 (2018) 1305–1322.

[26] T.Y. Hou, X.-H. Wu, A multiscale finite element method for elliptic problems in composite materials and porous media, J. Comput Phys. 134 (1) (1997) 169–189.

[27] Y. Efendiev, S. Lee, G. Li, J. Yao, N. Zhang, Hierarchical multiscale modeling for flows in fractured media using generalized multiscale finite element method, GEM-Inter. J. Geomath. 6 (2015) 141–162.

[28] P. Jenny, S.H. Lee, H.A. Tchelepi, Multi-scale finite-volume method for elliptic problems in subsurface flow simulation, J. Comput. Phys. 187 (1) (2003) 47–67.

[29] S.H. Lee, C. Wolfsteiner, H.A. Tchelepi, Multiscale finite-volume formulation for multiphase flow in porous media: black oil formulation of compressible, three-phase flow with gravity, Comput. Geosci. 12 (2008) 351–366.

[30] S.H. Lee, H. Zhou, H.A. Tchelepi, Adaptive multiscale finite-volume method for nonlinear multiphase transport in heterogeneous formations, J. Comput. Phys. 228 (24) (2009) 9036–9058.

[31] R. Künze, I. Lunati, An adaptive multiscale method for density-driven instabilities, J. Comput. Phys. 231 (17) (2012) 5557–5570.

[32] M. Cusini, C. van Kruijsdijk, H. Hajibeygi, Algebraic dynamic multilevel (ADM) method for fully implicit simulations of multiphase flow in porous media, J. Comput. Phys. 314 (2016) 60–79.

[33] M. Cusini, B. Fryer, C. van Kruijsdijk, H. Hajibeygi, Algebraic dynamic multilevel method for compositional flow in heterogeneous porous media, J. Comput. Phys. 354 (2018) 593–612.

[34] M. HosseiniMehr, M. Cusini, C. Vuik, H. Hajibeygi, Algebraic dynamic multilevel method for embedded discrete fracture model (F-ADM), J. Comput. Phys. 373 (2018) 324–345.

[35] M. Țene, M.S. Al Kobaisi, H. Hajibeygi, Algebraic multiscale method for flow in heterogeneous porous media with embedded discrete fractures (F-AMS), J. Comput. Phys. 321 (2016) 819–845.

[36] J.M. Nordbotten, M.A. Ferno, B. Flemisch, A.R. Kovscek, K.-A. Lie, The 11th society of petroleum engineers comparative solution project: problem definition, SPE J. 29 (05) (2024) 2507–2524.

[37] G.S.H. Pau, J.B. Bell, K. Pruess, A.S. Almgren, M.J. Lijewski, K. Zhang, High-resolution simulation and characterization of density-driven flow in CO_2 storage in saline aquifers, Adv. Water Resour. 33 (4) (2010) 443–455.

[38] M.L. Michelsen, J.M. Mollerup, Thermodynamic models: fundamentals & computational aspects, Tie-Line Publications Holte, Denmark, 2004.

[39] N. Spycher, K. Pruess, J. Ennis-King, CO_2-H_2O mixtures in the geological sequestration of CO_2. I. Assessment and calculation of mutual solubilities from 12 to 100 ˚c and up to 600bar, Geochim. Cosmochim. Acta 67 (16) (2003) 3015–3031.

[40] J.E. Garcia, Density of aqueous solutions of CO_2, Technical Report. LBNL (2001).

[41] Y. Wang, H. Hajibeygi, H.A. Tchelepi, Algebraic multiscale solver for flow in heterogeneous porous media, J. Comput. Phys. 259 (2014) 284–303.

[42] M.T. Elenius, J.M. Nordbotten, H. Kalisch, Convective mixing influenced by the capillary transition zone, Comput. Geosci. 18 (2014) 417–431.

[43] J.M. Nordbotten, M. Fernø, B. Flemisch, R. Juanes, M. Jørgensen, Final benchmark description: FluidFlower international benchmark study, 2022.

[44] E.W. Lemmon, Thermophysical properties of fluid systems, NIST chemistry WebBook (2010).

[45] H. Abdoulghafour, M. Sarmadivaleh, L.P. Hauge, M. Fernø, S. Iglauer, Capillary pressure characteristics of CO_2-brine-sandstone systems, Int. J. Greenhouse Gas Control 94 (2020) 102876.